

# Nonequilibrium transport through parallel double quantum dots in the Kondo regime

Y.-F. Yang and K. Held

Max-Planck-Institut für Festkörperforschung, 70569 Stuttgart, Germany

(Dated: December 2, 2024)

We extend a perturbative, nonequilibrium renormalization group approach to multi-orbital systems and apply it for studying transport through two parallel quantum dots coupled electrostatically. In general, the conductance shows pronounced Kondo-like peaks at three voltages. One of these peaks disappears if, as in some experiments, one of the dots is decoupled from one of the two leads. For an asymmetric coupling to the leads, also negative differential conductances are possible. This is a genuine nonequilibrium effect, accompanying the Kondo-like peaks. Moreover, a criterion to distinguish spin and orbital Kondo effect in such a system is discussed.

PACS numbers: 73.63.Kv, 71.27.+a, 72.10.Fk

## I. INTRODUCTION

Kondo physics in quantum dots has been under intense investigation in recent years. As was predicted theoretically,<sup>1,2</sup> the Kondo effect can lift the Coulomb blockade at low temperatures, leading to a conductance peak at zero bias.<sup>3</sup> In such experiments, often more than one orbital is involved. This is unavoidable, if the temperature or Kondo temperature is larger or comparable to the mean orbital splitting. Some nanostructures are also intentionally constructed in such a way, for example, two parallel quantum dots coupled electrostatically.<sup>4</sup> The latter allows for a controlled study of the interplay of spin and orbital (upper/lower dot) degrees of freedom.

On the theoretical side, the  $N$ -fold degenerate situation where all  $N$  (spin and orbital) levels of the Anderson model have the same one-particle energy  $\varepsilon$ , Coulomb interaction  $U$ , and hopping amplitude  $t$  to the leads is best understood. At strong coupling, the Schrieffer-Wolff transformation<sup>5</sup> then leads to the Coqblin-Schrieffer model<sup>6</sup> in terms of the exchange coupling  $J$ . This model has  $SU(N)$  symmetry for the rotation of orbitals and spins and, with increasing degeneracy  $N$ , leads to a strongly enhanced Kondo temperature  $T_K^{SU(N)} \approx D e^{-1/(N\rho_0 J)}$  ( $\rho_0$ : density of states in the leads;  $D$ : bandwidth of the leads;<sup>7</sup> we set  $k_B = \hbar = e = 1$  unless these constants appear explicitly in the equations).

Of course, we cannot expect a real quantum dot to have  $SU(N)$  symmetry. Quite an effort was devoted in the literature<sup>9,10,11,12,13</sup> to study the situation where either a magnetic field or a difference in orbital energy  $\delta$  splits  $N = 4$  levels into two doubly-degenerate subsets, hence breaking the  $SU(4)$  symmetry. If  $\delta \ll T_K^{SU(4)}$  the low-energy physics still resembles that of the  $SU(4)$ -symmetric model. In contrast for  $\delta \gg T_K^{SU(4)}$  one of the levels drops out of the scaling procedure; the low-energy physics is that of the usual  $SU(2)$ -symmetric Kondo model. In between, there is a crossover region.<sup>12</sup>

It is also unavoidable that the coupling constants  $J$  are orbital-dependent in experiment. Numerical renormalization group (NRG) calculations<sup>10,12</sup> suggest that for small enough  $\delta$  both orbitals are screened at the same

energy, in agreement with scaling analyses showing a robust (marginal)  $SU(4)$  fix point.<sup>12,13,14</sup>

So far, we only discussed equilibrium physics. A finite voltage  $V$  leads however to genuine nonequilibrium effects. For example, if  $V \approx \delta \gg T_K$  (the Kondo temperature) scattering between the two subsets of levels becomes relevant again. A Kondo-like resonance develops at  $V \approx \delta$ , visible e.g. as a peak in the conductance. But, at the same time, a genuine effect of nonequilibrium is the presence of decoherence processes induced by the finite current. This decoherence cuts off the flow to the strong coupling fix point even for temperatures  $T \ll T_K$ .<sup>2,15,16</sup> Then, physical quantities such as the differential conductance depend strongly on the configuration of the system like the asymmetry of the hopping  $t$  between quantum dot and leads.

Nonequilibrium Kondo physics is not as thoroughly investigated theoretically because standard approaches for the Anderson impurity model like NRG are not applicable. Rosch and coworkers<sup>17</sup> recently developed a perturbative, nonequilibrium renormalization group (RG) method to address nonequilibrium Kondo physics.<sup>18</sup> This approach is similar to Anderson's<sup>19</sup> poor man's scaling approach but includes nonequilibrium effects caused by the finite current through the system. In nonequilibrium, the low energy physics cannot be absorbed properly by a pure renormalization of the bare couplings. It is necessary to include the frequency dependence of the vertex functions.

In Section II, we extend the perturbative RG of Rosch *et al.*<sup>17</sup> to many orbitals, supplemented by the calculation of the decoherence rates in the Appendix. In Section III, we apply the method to the parallel double quantum dot system: Simplification of the RG Eqs. for this special case are discussed in Section III A. Results for the renormalized vertex, the decoherence rates and the nonequilibrium conductance for a symmetric coupling to the two leads are presented in Section III B. Asymmetric couplings to the two leads are addressed in Section III C. Here, negative differential conductances are possible. In addition, the linear (equilibrium) conductance is analyzed in Section III D. A summary of the results can be found in Section IV.

## II. NONEQUILIBRIUM PERTURBATIVE RG

Starting point for modeling a quantum dot with  $N$ -levels should be the Anderson impurity model:

$$H_{\text{AIM}} = H_0 + \sum_{\lambda mk} (t_{\lambda m} c_{mk\lambda}^+ d_m + \text{H.c.}) + \sum_m \epsilon_m d_m^+ d_m + \sum_{m \neq m'} U_{mm'} n_m n_{m'}. \quad (1)$$

Here  $d_m^+$  and  $d_m$  ( $c_{mk\lambda}^+$  and  $c_{mk\lambda}$ ) are creation and annihilation operators for electrons in the dot (lead  $\lambda$ );  $n_m = d_m^+ d_m$ ;  $\epsilon_m$  describes the one-particle energy of level  $m$  with  $m = \{\sigma, i\}$  subsuming the spin and orbital index;  $U_{mm'}$  is the Coulomb repulsion within the dot. The levels of the dot hybridize via  $t_{\lambda m}$  with non-interacting leads  $\lambda$  described by (later, we simplify  $\epsilon_{\lambda mk} = \epsilon_k$ )

$$H_0 = \sum_{\lambda mk} \epsilon_{\lambda mk} c_{\lambda mk}^+ c_{\lambda mk}. \quad (2)$$

In this paper, we assume each quantum dot level  $m$  to couple to its own lead channel which is for example the case if the different levels correspond to different quantum dots like in Ref. 4 (see also Figure 4 of the present paper as an illustration). But in other situations it is possible to move an electron phase coherently from one level  $m$  via the leads to another level  $m'$ . This goes beyond Hamiltonian (1).

While the Anderson impurity model allows us to make contact with experiment (estimating parameters), we address in the following the parameter regime  $\epsilon_m \ll \mu_\lambda \ll U_{mm'} + \epsilon_m$  for all  $m, m', \lambda$  ( $\mu_\lambda$ : chemical potential in lead  $\lambda$ ) so that charge fluctuations are suppressed. Then, with  $\sum_m \langle n_m \rangle = 1$  electron within the dot, we can map Hamiltonian (1) onto the subspace with one electron in the dot by a Schrieffer-Wolff transformation,<sup>5</sup> i.e., onto the general effective Kondo Hamiltonian (neglecting a potential scattering term)

$$H = H_0 + \sum_m \epsilon_m X^{mm} + \sum_{\lambda_1 m_1 k_1; \lambda_2 m_2 k_2} (J_{m_1 m_2}^{\lambda_1 \lambda_2} X^{m_1 m_2} c_{\lambda_2 m_2 k_2}^+ c_{\lambda_1 m_1 k_1} + \tilde{J}_{m_1 m_2}^{\lambda_1 \lambda_2} X^{m_1 m_1} c_{\lambda_2 m_2 k_2}^+ c_{\lambda_1 m_2 k_1}). \quad (3)$$

Here, the Hubbard operators<sup>20</sup>  $X^{m_1 m_2}$  represent the scattering of the local state from level  $m_2$  to level  $m_1$ . When the lead's band edge  $D > |\epsilon_m|$ , the local level  $\epsilon_m$  of the Anderson impurity model is renormalized to  $\epsilon_m$  in the Kondo model;<sup>8</sup>  $J_{m_1 m_2}^{\lambda_1 \lambda_2} = t_{\lambda_1 m_1}^* t_{\lambda_2 m_2} (\frac{1}{U_{m_1 m_2} + \epsilon_d} - \frac{1}{\epsilon_d})$  and  $\tilde{J}_{m_1 m_2}^{\lambda_1 \lambda_2} = (1 - 2\delta_{m_1 m_2}) t_{\lambda_1 m_2}^* t_{\lambda_2 m_2} \frac{1}{U_{m_1 m_2} + \epsilon_d}$  where  $\epsilon_d$  is the average level energy, neglecting the level splitting which is much smaller than  $U, \epsilon_d$ . Note, that for  $m_1 = m_2$  both  $J$  and  $\tilde{J}$  yield the same kind of contribution. The advantage of having this term twice (i.e., distributed to  $\tilde{J}_{m_1 m_1}^{\lambda_1 \lambda_2}$  and  $J_{m_1 m_1}^{\lambda_1 \lambda_2}$ ) is the simplification of the following equations. The same distribution of the  $m_1 = m_2$  contribution is usually also employed for the Coqblin-Schrieffer model which is the SU(N) symmetric version of Hamiltonian (3) [ $J$  and  $\tilde{J} = J/N$  are then level-independent].<sup>6</sup>

Let us now generalize the perturbative RG approach of Ref. 17 to the multi-orbital Hamiltonian (3). The base quantity is the vertex function which -at finite voltages or currents- becomes frequency dependent. Like in the poor man's scaling approach, we integrate out high energy degrees of freedom in the intervals  $[-D, -D + |dD|]$  and  $[D - |dD|, D]$ , resulting in a renormalization of the vertex. The Feynman diagrams for this renormalization are shown in Figure 1 to lowest order (one-loop RG). To directly apply standard perturbation theory, the localized states of the Anderson impurity model can be expressed by pseudo Fermions, see Ref. 17. Starting point of the RG scheme is the unrenormalized  $k$ -independent vertex

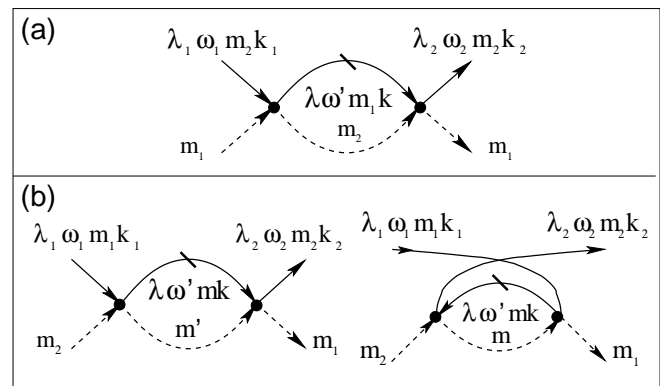


FIG. 1: One-loop Feynman diagrams for the renormalization of the vertex functions (a)  $\tilde{g}_{m_1 m_2}^{\lambda_1 \lambda_2}(\omega)$  and (b)  $g_{m_1 m_2}^{\lambda_1 \lambda_2}(\omega)$ . The full line denotes the electron and the dashed the localized state of the Kondo model. Note that the second (hole) diagram of (b) does not contribute for (a) since it cancels with the corresponding first (particle) diagram. For the vertex renormalization, the electron line is restricted to a small interval  $|dD|$  at the band edges, as indicated by the dash.

$g_{m_1 m_2}^{\lambda_1 \lambda_2}(\omega) = \rho_0 J_{m_1 m_2}^{\lambda_1 \lambda_2}$ ,  $\tilde{g}_{m_1 m_2}^{\lambda_1 \lambda_2}(\omega) = \rho_0 \tilde{J}_{m_1 m_2}^{\lambda_1 \lambda_2}$ , where we neglect the energy dependence of  $\rho_0$ . Here, the frequency of the localized state is approximated by  $\epsilon_m$  so that the vertex depends only on one  $\omega$  (the average of incoming and outgoing electron frequency). This is only possible in the weak coupling regime.

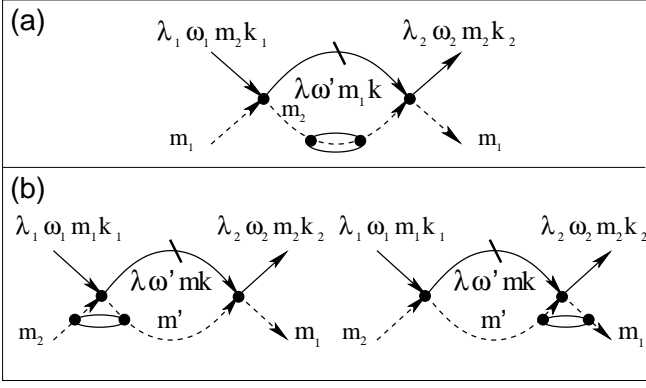


FIG. 2: Vertex corrections and self energy diagrams beyond the one-loop approximation of Figure 1.

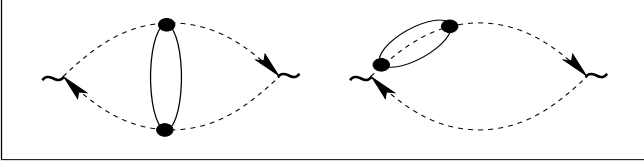


FIG. 3: A similar combination of vertex corrections and self energy diagrams as in Figure 2 emerges if we calculate generalized spin/orbit susceptibilities.

For the nonequilibrium situation, the calculation of the diagrams of Figure 1 requires in principle the usage of Keldysh<sup>21</sup> Green functions. Rosch *et al.*<sup>17</sup> argued however that, to leading order in  $1/\ln(V/T_K)$ , it is sufficient to keep track of the real part of  $g_{m_1 m_2}^{\lambda_1 \lambda_2}(\omega)$ , as indicated by perturbation theory.<sup>22</sup> This gives rise to the same kind of vertex renormalization per energy interval  $\ln D$  as in the poor man's scaling approach, i.e. at  $T = 0$ :

$$\frac{1}{2} \frac{\partial}{\partial \ln D} \int_{-D}^D d\epsilon \frac{\text{sign}(\epsilon)}{\epsilon - \Delta\omega}. \quad (4)$$

Here,  $\Delta\omega$  is given by the chemical potential and the change of energy of the localized state in Figure 1. A finite temperature, smears out the sharp step of the in-

tegrand in Eq. (4), cutting off the emerging logarithm. Another cut-off is induced by the finite voltage, driving the system out of equilibrium. This nonequilibrium effect originates from higher order diagrams such as those of Figure 2. These diagrams give rise to an imaginary part of the self energy and vertex corrections, even at low  $\omega$ 's for the nonequilibrium situation. Generally, this will result in the following modification of the pole in Eq. (4):

$$\frac{1}{2} \frac{\partial}{\partial \ln D} \int_{-D}^D d\epsilon \frac{\text{sign}(\epsilon)}{\epsilon - \Delta\omega + i\gamma \text{sign}(\epsilon)} \approx \Theta(D - \sqrt{\Delta\omega^2 + \gamma^2}) \equiv \Theta_{\Delta\omega}^{\gamma}, \quad (5)$$

where  $\Theta(x) = 1(0)$  for  $x \geq 0 (< 0)$ .

For the proper calculation of the low energy cut-off  $\gamma$ , we would need to calculate diagrams as in Figure 2. This goes beyond the scope of the present paper. As in Ref. 17, we follow a heuristic approach instead. To this end, first note that similar combinations of vertex corrections and self energy inclusions occur when calculating generalized susceptibilities for level  $m_1$  and  $m_2$ ; see Figure 3. Secondly, an incorrect prefactor of  $\gamma$  is not affecting the results to leading order in  $1/\ln(V/T_K)$ . Hence, we can crudely estimate  $\gamma$  by the decoherence rates  $\gamma_{m_1 m_2}$  of the corresponding susceptibilities. For example, we can take the maximal  $\gamma_{m_1 m_2}$  of the levels involved (or temperature if higher):  $\gamma \equiv \gamma_{m_1 m_2 m_3} = \max\{T, \gamma_{m_1 m_2}, \gamma_{m_2 m_3}\}$  where  $m_1, m_2$  and  $m_3$  denote the incoming, intermediate, and final local state. In our calculation for two levels in Section III with SU(2) spin symmetry, only two of the orbitals  $i$  ( $m = \{\sigma, i\}$ ) can be different, and the vertices are symmetric w.r.t. the spin indices. We then actually use the intra-orbital rate  $\gamma = \max\{T, \gamma_{ii} \equiv \gamma_i\}$  as a cut-off for diagrams where only one orbital is involved and the inter-orbital  $\gamma = \max\{T, \gamma_{12}\}$  whenever both orbitals are involved. The calculation of  $\gamma_{m_1 m_2}$  via the susceptibilities is presented in the Appendix.

Having identified the cut-off  $\gamma_{m_1 m_2 m_3}$ , we can now write down the RG equation for the vertex functions  $\tilde{g}_{m_1 m_2}^{\lambda_1 \lambda_2}(\omega)$  and  $g_{m_1 m_2}^{\lambda_1 \lambda_2}(\omega)$ , corresponding to Figure 1:

$$\begin{aligned} \frac{\partial \tilde{g}_{m_1 m_2}^{\lambda_1 \lambda_2}(\omega)}{\partial \ln D} &= \sum_{\lambda} g_{m_2 m_1}^{\lambda_1 \lambda} \left( \omega + \frac{\epsilon_{m_1} - \epsilon_{m_2}}{2} \right) g_{m_1 m_2}^{\lambda \lambda_2} \left( \omega + \frac{\epsilon_{m_1} - \epsilon_{m_2}}{2} \right) \Theta_{\omega + \epsilon_{m_1} - \epsilon_{m_2} - \mu_{\lambda}}^{\gamma_{m_2 m_1 m_2}}, \\ \frac{\partial g_{m_1 m_2}^{\lambda_1 \lambda_2}(\omega)}{\partial \ln D} &= - \sum_{m\lambda} g_{m_1 m}^{\lambda_1 \lambda} \left( \omega - \frac{\epsilon_{m_2} - \epsilon_m}{2} \right) g_{m m_2}^{\lambda \lambda_2} \left( \omega - \frac{\epsilon_{m_1} - \epsilon_m}{2} \right) \Theta_{\omega - (\epsilon_{m_1} + \epsilon_{m_2} - 2\epsilon_m)/2 - \mu_{\lambda}}^{\gamma_{m_2 m m_1}} \\ &\quad + \sum_{\lambda} g_{m_1 m_2}^{\lambda_1 \lambda}(\omega) \left[ \tilde{g}_{m_1 m_2}^{\lambda \lambda_2} \left( \omega - \frac{\epsilon_{m_1} - \epsilon_{m_2}}{2} \right) \Theta_{\omega - (\epsilon_{m_1} - \epsilon_{m_2})/2 - \mu_{\lambda}}^{\gamma_{m_2 m_1 m_1}} - \tilde{g}_{m_2 m_2}^{\lambda \lambda_2} \left( \omega - \frac{\epsilon_{m_1} - \epsilon_{m_2}}{2} \right) \Theta_{\omega - (\epsilon_{m_1} - \epsilon_{m_2})/2 - \mu_{\lambda}}^{\gamma_{m_2 m_2 m_1}} \right] \\ &\quad + \sum_{\lambda} g_{m_1 m_2}^{\lambda \lambda_2}(\omega) \left[ \tilde{g}_{m_2 m_1}^{\lambda_1 \lambda} \left( \omega + \frac{\epsilon_{m_1} - \epsilon_{m_2}}{2} \right) \Theta_{\omega + (\epsilon_{m_1} - \epsilon_{m_2})/2 - \mu_{\lambda}}^{\gamma_{m_2 m_2 m_1}} - \tilde{g}_{m_1 m_1}^{\lambda_1 \lambda} \left( \omega + \frac{\epsilon_{m_1} - \epsilon_{m_2}}{2} \right) \Theta_{\omega + (\epsilon_{m_1} - \epsilon_{m_2})/2 - \mu_{\lambda}}^{\gamma_{m_2 m_1 m_1}} \right]. \end{aligned} \quad (6)$$

The equation for  $\tilde{g}$  can be obtained from Figure 1a. The

first line of the equation for  $g$  corresponds to the right

diagram of Figure 1b; the second and third line stem from the particle and the hole diagram of Figure 1b with  $m = m_2$  and  $m = m_1$ , respectively. Note that the different frequencies of Figure 1 are related by energy conservation and that  $\omega = (\omega_1 + \omega_2)/2^{23}$ . The  $k$ -integration (note that  $k$  is not conserved) over the band edge states results in a factor  $\rho_0$  which is already included in  $g$ . The electron states in the leads range to  $\pm D$  relative to the respective chemical potential  $\mu_\lambda$ .

The renormalized vertex functions of Eq. (6) have to be calculated self-consistently together with  $\gamma_{mm'}$  [Eq. (A7) of the Appendix] which determine the cut-offs  $\gamma_{m_1 m_2 m_3}$ .

### Conductance

To study the most important physical quantity, the conductance, we employ the scattering T-matrix  $\hat{T}_{m_1 m_2}^{\lambda_1 \lambda_2}(k_1, k_2)$  for the process moving an electron from state  $\{k_1 m_1\}$  in lead  $\lambda_1$  to state  $\{k_2 m_2\}$  in lead  $\lambda_2$ . This process necessarily also involves the local state which changes in the opposite direction. The change of the local state can be expressed via spin and orbital operators in the T-matrix (see e.g. Ref. 8). By  $\langle |\hat{T}_{m_1 m_2}^{\lambda_1 \lambda_2}(k_1, k_2)|^2 \rangle$ , we then denote the thermal average of the T-matrix w.r.t. the local state configurations. The steady state condition requires in terms of this averaged T-matrix:

$$\begin{aligned} \sum_{\lambda_1 \lambda_2; k_1 k_2} \langle |\hat{T}_{m_1 m_2}^{\lambda_1 \lambda_2}(k_1, k_2)|^2 \rangle f_{\lambda_1}(\epsilon_{k_1}) [1 - f_{\lambda_2}(\epsilon_{k_2})] = \\ \sum_{\lambda_1 \lambda_2; k_1 k_2} \langle |\hat{T}_{m_2 m_1}^{\lambda_2 \lambda_1}(k_2, k_1)|^2 \rangle f_{\lambda_2}(\epsilon_{k_2}) [1 - f_{\lambda_1}(\epsilon_{k_1})], \quad (7) \end{aligned}$$

where  $f_\lambda(\epsilon) = 1/(e^{\beta(\epsilon - \mu_\lambda)} + 1)$  is the Fermi function for lead  $\lambda$ . A difference to Ref. 17,26 is that we do not take into account a  $\gamma$ -broadening of the spectral function. This is effectively described by a broadening of the Fermi functions in Ref. 17,26, resulting in corrections to subleading order in  $1/\ln(V/T_K)$ .

Since we consider the situation where either the voltage-induced decoherence rate or the temperature is larger than the Kondo temperature the renormalization process is cut off, instead of flowing to strong coupling. Therefore, we are at weak coupling and we can calculate the scattering matrix in lowest order:  $\hat{T}_{m_1 m_2}^{\lambda_1 \lambda_2}(k_1, k_2) = \langle \lambda_2 m_2 k_2 | H_{\text{int}} | \lambda_1 m_1 k_1 \rangle$ , where  $H_{\text{int}}$  denotes the interaction between the lead electrons and the local states via  $J$  and  $\bar{J}$ , i.e., the last two terms of Eq. (3). Averaged over the local states, this yields:

$$\begin{aligned} \langle |\hat{T}_{m_1 m_2}^{\lambda_1 \lambda_2}(k_1, k_2)|^2 \rangle = (1 - \delta_{m_1 m_2}) \langle n_{m_2} \rangle g_{m_1 m_2}^{\lambda_1 \lambda_2}(\omega)^2 / \rho_0^2 \\ + \delta_{m_1 m_2} \sum_{m \neq m_1} \langle n_m \rangle \tilde{g}_{m_1 m}^{\lambda_1 \lambda_2}(\omega)^2 / \rho_0^2 \\ + \delta_{m_1 m_2} \langle n_{m_1} \rangle (g_{m_1 m_2}^{\lambda_1 \lambda_2}(\omega) + \tilde{g}_{m_1 m_2}^{\lambda_1 \lambda_2}(\omega))^2 / \rho_0^2. \quad (8) \end{aligned}$$

Here, we have replaced the bare coupling by the renormalized one, i.e.,  $J \rightarrow g(\omega)/\rho_0$  with  $\omega \equiv (\epsilon_k + \epsilon_{k'})/2$ ;  $\langle n_m \rangle$  is the average occupation of local level  $m$ .

In a first step  $g$  and  $\tilde{g}$  are calculated by Eq. (6), which is solved self-consistently together with the cut-off  $\gamma_{m_1 m_2}$  [Eq. (A7)]. With these  $g$ 's and  $\tilde{g}$ 's, the occupations  $\langle n_m \rangle$  can be determined via Eqs. (7) and (8) and the constraint  $\sum_m \langle n_m \rangle = 1$ .

From the T-matrix [Eq. (8)], we can then calculate the current from lead  $\lambda$  and orbital  $m$  as the difference between scattering out of and into the lead:

$$\begin{aligned} I_{\lambda m} = -2\pi \sum_{\substack{\lambda' m' (\neq \lambda m) \\ k k'}} \delta(\epsilon_k - \epsilon_{k'} + \epsilon_{m'} - \epsilon_m) \\ \{ f_\lambda(\epsilon_k) [1 - f_{\lambda'}(\epsilon_{k'})] \langle |\hat{T}_{m m'}^{\lambda \lambda'}(k, k')|^2 \rangle \\ - f_{\lambda'}(\epsilon_{k'}) [1 - f_\lambda(\epsilon_k)] \langle |\hat{T}_{m' m}^{\lambda' \lambda}(k', k)|^2 \rangle \}. \quad (9) \end{aligned}$$

The differential conductance follows as  $G_{\lambda m} = \partial I_{\lambda m} / \partial V$ .

## III. TWO PARALLEL QUANTUM DOTS

Let us now apply the perturbative RG equations to the situation of two parallel quantum dots each coupled to two leads, see Figure 4. This corresponds to  $m = \{i, \sigma\}$  with  $\sigma = \uparrow (+), \downarrow (-)$  denoting the spin and  $i = 1(+), 2(-)$  the two dots (orbitals) with level energy  $\epsilon_{\{i\sigma\}} = -i\delta/2$  ( $\bar{i} = -i$  in the following).

### A. Simplification of the RG Eq.

Due to the SU(2) spin symmetry in each dot, we can reduce the number of vertices we have to deal with. Furthermore, some of the vertices are connected via scaling invariants. Altogether this allows for the following reduction of vertices:  $g_{i\sigma; i\sigma'}^{\lambda\lambda'}(\omega) \equiv g_i^{\lambda\lambda'}(\omega)/2$ ,  $g_{i\sigma; \bar{i}\sigma'}^{\lambda\lambda'}(\omega) \equiv g_{12}^{\lambda\lambda'}(\omega)/2$ ,  $\tilde{g}_{i\sigma; \bar{i}\sigma'}^{\lambda\lambda'}(\omega) \equiv -\tilde{g}_i^{\lambda\lambda'}(\omega)/4$ , and -from the scaling

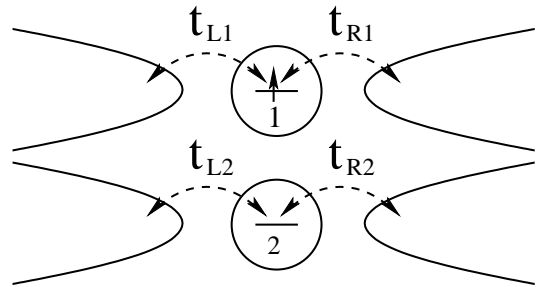


FIG. 4: Sketch of the parallel double quantum dot configuration. Each dot is coupled to its own leads. For the Anderson impurity model, this coupling is described by hopping processes  $t_{\lambda i}$ ; there are intra-dot and inter-dot Coulomb repulsions  $U_{ii'}$  which are not indicated in the Figure. We study here the corresponding Kondo model which is restricted to the subspace with one electron in the dot. Then,  $g_{ii'}^{\lambda\lambda'}$  describes the combination of two hopping processes, leaving the number of electrons in the dot unchanged.

invariants-  $\tilde{g}_{i\sigma;i\sigma'}^{\lambda\lambda'}(\omega) = (\tilde{g}_i^{\lambda\lambda'}(\omega) - g_i^{\lambda\lambda'}(\omega))/4$ . The meaning of the redefined vertices becomes clear if we write the Hamiltonian in terms of the coupling constants  $J_{i(12)}$  and  $\tilde{J}$  corresponding to  $g_{i(12)}$  and  $\tilde{g}$ :

$$\begin{aligned}
H = & \sum_{\lambda i \sigma k} (\epsilon_k - \mu_\lambda) c_{\lambda i \sigma k}^+ c_{\lambda i \sigma k} - \frac{\delta}{2} (n_1 - n_2) \\
& + \sum_{\lambda \lambda' i \sigma \sigma' k k'} \frac{J_i^{\lambda \lambda'}}{2} \mathbf{S}_i \cdot c_{\lambda i \sigma k}^+ \boldsymbol{\tau}_{\sigma \sigma'} c_{\lambda' i \sigma' k'} \\
& + \sum_{\lambda \lambda' \sigma \sigma' k k'} \frac{J_{12}^{\lambda \lambda'}}{2} (X^{\{1\sigma'\}\{2\sigma\}} c_{\lambda 2 \sigma k}^+ c_{\lambda' 1 \sigma' k'} + \text{H.c.}) \\
& + (n_1 - n_2) \sum_{\lambda \lambda' \sigma k k'} \frac{\tilde{J}^{\lambda \lambda'}}{4} (c_{\lambda 1 \sigma k}^+ c_{\lambda' 1 \sigma k'} - c_{\lambda 2 \sigma k}^+ c_{\lambda' 2 \sigma k'}).
\end{aligned} \quad (10)$$

Here,  $\mathbf{S}_i$  denotes the spin operators in orbital  $i$ ,  $\boldsymbol{\tau}$  the vector of Pauli matrices, and  $n_i = \sum_{\sigma} n_{i\sigma}$ . Note that with only one electron in the dots, there is no need to consider Hund's coupling.

Using the SU(2) symmetries in both orbitals and the above scaling invariants, the scaling Eq. (6) become particularly simple for a symmetric coupling to the leads (then,  $g_i(\omega)$ ,  $\tilde{g}_i(\omega)$ , and  $g_{12}(\omega)$  do not depend on the lead indices; we can hence drop the  $\lambda, \lambda'$  indices):

$$\begin{aligned}
\frac{\partial g_i(\omega)}{\partial \ln D} &= - \sum_{\lambda=\pm 1} [g_i^2(\omega) \Theta_{\omega+\lambda V/2}^{\gamma_i} + g_{12}^2(\omega + \frac{i\delta}{2}) \Theta_{\omega+i(\delta+\lambda V/2)}^{\gamma_{12}}], \\
\frac{\partial g_{12}(\omega)}{\partial \ln D} &= -g_{12}(\omega) \sum_{i;\lambda=\pm 1} [\frac{3}{4} g_i(\omega - \frac{i\delta}{2}) + \frac{1}{2} \tilde{g}_i(\omega - \frac{i\delta}{2})] \Theta_{\omega + \frac{\lambda V - i\delta}{2}}^{\gamma_{12}}, \\
\frac{\partial \tilde{g}_i(\omega)}{\partial \ln D} &= - \sum_{\lambda=\pm 1} g_{12}^2(\omega + i\delta/2) \Theta_{\omega+i(\delta+\lambda V/2)}^{\gamma_{12}}.
\end{aligned} \quad (11)$$

Eq. (11) has to be solved self-consistently together with the decoherence rates of the Appendix which simplify for the parallel double dot system to:

$$\begin{aligned}
\gamma_i = \pi \sum_{\lambda \lambda'} \int d\omega \{ & g_i^2(\omega) f_\lambda(\omega) [1 - f_{\lambda'}(\omega)] \\
& + g_{12}^2(\omega) f_\lambda(\omega + i\frac{\delta}{2}) [1 - f_{\lambda'}(\omega - i\frac{\delta}{2})] \} \quad (12)
\end{aligned}$$

$$\begin{aligned}
\gamma_{12} = \frac{\pi}{2} \sum_{\lambda \lambda' i} \int d\omega \{ & [\frac{3}{4} g_i^2(\omega) + \tilde{g}_i^2(\omega)] f_\lambda(\omega) [1 - f_{\lambda'}(\omega)] \\
& + g_{12}^2(\omega) f_\lambda(\omega + i\frac{\delta}{2}) [1 - f_{\lambda'}(\omega - i\frac{\delta}{2})] \} \quad (13)
\end{aligned}$$

These  $\gamma_i$ , or  $T$  for  $T > \gamma_i$ , cut off the  $\Theta$ -functions in Eq. (11).

The equations for the occupations [Eq. (7), taking  $m_1 = m_2$  in Eq. (8)] and the current [Eq. (9)] reduce to

$$\langle n_i \rangle \sum_{\lambda, \lambda'} \int d\epsilon g_{12}^2(\epsilon - i\frac{\delta}{2}) f_\lambda(\epsilon) [1 - f_{\lambda'}(\epsilon - i\delta)] = (i \rightarrow \bar{i}) \quad (14)$$

and

$$\begin{aligned}
I_{i\sigma} = \frac{\pi}{8} \int d\omega \{ & [3\langle n_i \rangle g_i^2(\omega) + \tilde{g}_i^2(\omega)] [f_L(\omega) - f_R(\omega)] \\
& + 4\langle n_{\bar{i}} \rangle g_{12}^2(\omega + i\delta/2) f_L(\omega) [1 - f_R(\omega + i\delta)] \\
& - 4\langle n_i \rangle g_{12}^2(\omega - i\delta/2) f_R(\omega) [1 - f_L(\omega - i\delta)] \\
& + 4\langle n_{\bar{i}} \rangle g_{12}^2(\omega + i\delta/2) f_L(\omega) [1 - f_L(\omega + i\delta)] \\
& - 4\langle n_i \rangle g_{12}^2(\omega - i\delta/2) f_L(\omega) [1 - f_L(\omega - i\delta)] \},
\end{aligned} \quad (15)$$

respectively. In Eq. (15), the first line stems from the current from left channel  $i$  to right channel  $i$ . The 2nd and 3rd (4th and 5th) line correspond to the current to right (left) channel  $\bar{i}$ . The latter are balanced by similar terms from the right lead so that the net current from one orbital to the other is zero.

## B. Nonequilibrium transport

Let us now discuss the numerical solution for the renormalized vertex functions of Eq. (6)/(11) which is presented in Figure 5. This vertex function, a frequency-dependent renormalization of the interactions  $J, \tilde{J}$  between lead electrons and local states in the quantum dot, is the fundamental theoretical quantity; it is not directly observable experimentally, but -together with the occupations- allows to calculate e.g. the current which will be discussed later. In the following, all energies are normalized to the (equilibrium) Kondo temperature for  $\delta = 0$ , i.e., to  $T_K^0 = T_K(\delta = 0)$ .<sup>24</sup> Due to the finite voltage  $V$  applied, the two leads are thermalized by two different Fermi functions with  $\mu_L = \mu + V/2$  and  $\mu_R = \mu - V/2$ , respectively. The quantum dot is out of equilibrium.

Here and in the following figures, the initial coupling constants which are not explicitly mentioned follow from the ones of the Figure caption since they stem from the same  $t$ 's of the Anderson impurity. For example,  $g_{12}^{LR} = g_{12}^{LL} \sqrt{g_1^{RR}/g_1^{LL}}$ . We always set  $\tilde{g}_i^{\lambda\lambda'} = 0$  initially.

To understand the four peak structure of Figure 5, it is instructive to integrate Eq. (11) analytically, dividing the Eqs. by the squared coupling constant from the left hand side (e.g. multiplying the first line by  $1/g_i^2(\omega)$ ) and afterwards keeping the  $g$ 's on the right hand side constant (at the initial values). This is justified as long as the renormalization of the vertex functions stays small. But our mere aim here is to understand the positions and widths of the different peaks. From Eq. (11) we straightforwardly get in this way:

$$g_i(\omega) \sim \frac{1}{\sum_{\lambda} (\ln \frac{|\omega + \lambda V/2|_i}{T_k^0} + \ln \frac{|\omega + i(\delta + \lambda V/2)|_{12}}{T_k^0})}, \quad (16)$$

$$g_{12}(\omega) \sim \frac{1}{\sum_{i,\lambda} \ln \frac{|\omega + \frac{(\lambda V - i\delta)}{2}|_{12}}{T_k^0}}, \quad (17)$$

$$\tilde{g}_i(\omega) \sim \frac{1}{\sum_{\lambda} \ln \frac{|\omega + i(\delta + \lambda V/2)|_{12}}{T_k^0}}, \quad (18)$$

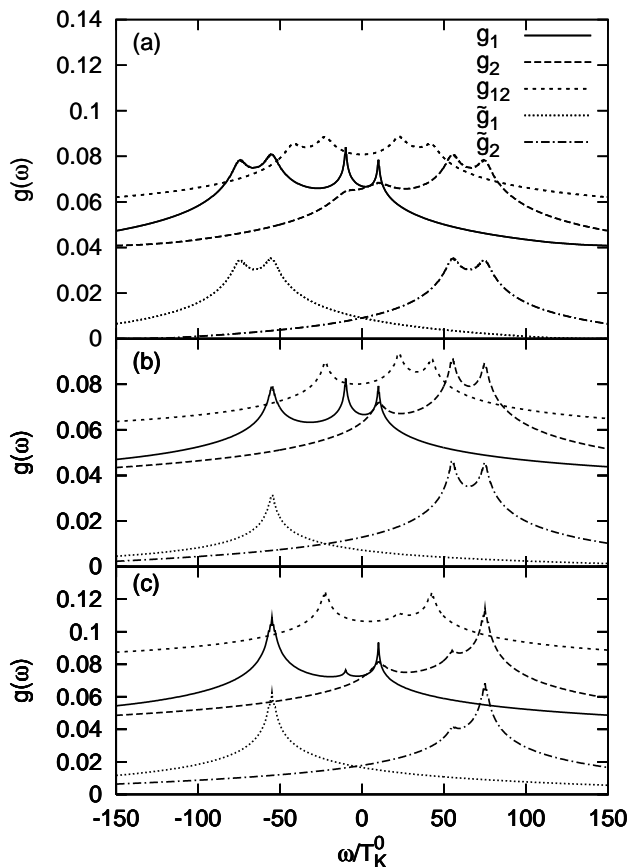


FIG. 5: Renormalized vertex functions to the left lead at  $T/T_K^0 = 0.5$ ,  $V/T_K^0 = 20$ ,  $\delta/T_K^0 = 65$  ( $g_{i(12)}$  in the legend box stands for  $g_{i(12)}^{LL}$ ). Part a) is for symmetric initial couplings  $g_i^{\lambda\lambda'} = 0.04$ ,  $g_{12}^{\lambda\lambda'} = 0.06$  for all  $\lambda, \lambda'$ . In part b) the right lead of dot 2 was removed, i.e., parameters as in a) except for  $g_{2(12)}^{RR} = g_{2(12)}^{LR} = 0$ . In part c) also the coupling of dot 1 is asymmetric:  $g_1^{LL} = 0.04$ ,  $g_1^{RR} = 0.06$ ,  $g_2^{LL} = 0.04$ ,  $g_2^{RR} = 0$ ,  $g_{12}^{LL} = 0.08$ .

where  $|\omega|_i \equiv \sqrt{\omega^2 + \max\{\gamma_i, T\}}$ , and prefactors of order one (like  $g_{12}/g_i$ ) before the logarithmic terms are neglected.

By means of Eq. (16), we can now identify the origin of the four Kondo-like peaks in the  $g_i$ 's seen in Figure 5. When the frequency matches the difference to the left or right Fermi level ( $\omega = \pm V/2$ ) a single dot (spin) Kondo-like resonance develops; but the flow to strong coupling is cut off by the corresponding decoherence rate  $\gamma_i$  (or  $T$ ). The other two peaks in  $g_i$  stem from the orbital Kondo effect. Here, the localized state changes to the other orbital and back to the original orbital. These processes are enhanced if the conduction electron scatters to the Fermi level of the left or right lead, requiring  $\omega = -i\delta \pm V/2$ . Hence the resonances [and those of Eq. (18)] are at  $\omega = -i\delta \pm V/2$  and the cut-off is  $\gamma_{12}$ . Similarly, the peaks for  $g_{12}(\omega)$  in Eq. (17) are at  $\pm \frac{V \pm \delta}{2}$  (with  $\delta/2$  instead of  $\delta$  since  $\omega$  is the average of incoming and

outgoing frequency which differ by  $\delta$  as  $g_{12}$  changes the orbital).

In part b) of Figure 5 the right lead of dot 2 was removed. As scattering to the removed lead is now prohibited, one out of four peaks disappears for  $g_i$  and  $g_{12}$ . The missing peak is the one at the lowest value of  $\omega$  in part a). We can hence identify the missing peak with spin ( $g_2$ ) and orbital scattering processes ( $g_1$  and  $g_{12}$ ) via the right lead of dot 2. Part c) of Figure 5 is for the situation where also dot 1 is coupled asymmetrically. Some peaks are clearly suppressed.

Figure 6 shows the three decoherence rates  $\gamma_1$ ,  $\gamma_2$ , and  $\gamma_{12}$  which need to be calculated self-consistently together with the RG Eqs. As in Eqs. (16)-(18) it is instructive to calculate  $\gamma$  from the unrenormalized  $g$ 's (not self-consistently/in lowest order approximation). At large orbital splitting  $|\delta| \gg \max\{T, \frac{|V|}{4}\}$ , this yields for symmetric coupling to left/right lead (Figure 6 around zero):

$$\begin{aligned} \gamma_1 &\approx 4\pi g_1^2 \max\left\{T, \frac{|V|}{4}\right\}, \\ \gamma_2 &\approx 4\pi g_{12}^2 |\delta|, \\ \gamma_{12} &\approx 2\pi g_{12}^2 |\delta|. \end{aligned} \quad (19)$$

The decoherence rate for dot 2, i.e.,  $\gamma_2$ , and the intra-orbital rate  $\gamma_{12}$  are both proportional to  $|\delta|$  as there are many decoherence processes, reflecting the instability of the high energy level of dot 2. Decoherence processes for dot 1 on the other hand become only available at finite bias voltages. For very large  $|\delta| \gg T_K^0$ , the system shows the usual single-orbital (spin) Kondo effect. Note that, for small  $V$ , we have  $\gamma_1 < T_K^0$ . One might envisage that this signals a flow to strong coupling and, hence, a breakdown of the RG Eqs. However, for the large splitting  $\delta$  the real Kondo temperature is very much reduced. It actually is only  $\approx 1/100 T_K^0$  here, much smaller than the cut-off.

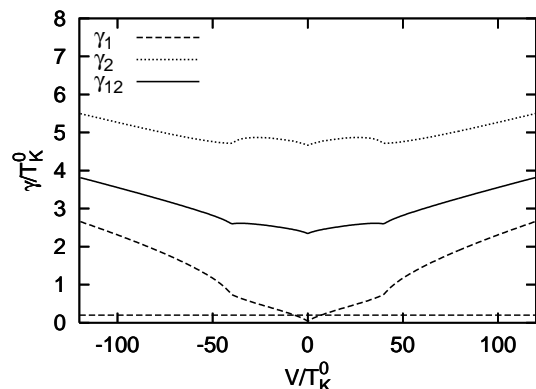


FIG. 6: Scattering rates as a function of bias voltage  $V$  at  $T/T_K^0 = 0.2$  and  $\delta/T_K^0 = 40$ . The initial couplings are symmetric:  $g_1^{\lambda\lambda'} = 0.04$ ,  $g_2^{\lambda\lambda'} = 0.01$ ,  $g_{12}^{\lambda\lambda'} = 0.06$ . For large bias voltage, the scattering rates are larger than  $T$  (dashed line) but much smaller than  $V$ .

Let us now discuss the large voltage range of Figure 6. For  $|V| \gg |\delta|$ , all curves show a similar asymptotic behavior:

$$\begin{aligned}\gamma_i &\approx 4\pi[(g_i)^2 + (g_{12})^2] \max\{T, \frac{|V|}{4}\}, \\ \gamma_{12} &\approx 2\pi \sum_i [\frac{3}{4}(g_i)^2 + (\tilde{g}_i)^2 + (g_{12})^2] \max\{T, \frac{|V|}{4}\}.\end{aligned}\quad (20)$$

While all  $\gamma_i$ 's are now proportional to  $|V|$ , we see in Figure 6 that nonetheless  $\gamma_i \ll |V|$ . This is due to the small prefactors  $\sim g^2$  in Eq. (20). The current which has similar prefactors causes the decoherence processes. For sufficiently large  $V$ , all  $\gamma_i$ 's become larger than temperature; the current induced decoherence exceeds the temperature effect.

In between the two extremes  $|V| \ll |\delta|$  and  $|V| \gg |\delta|$ , the transition from a strong orbital decoherence rate of dot 2 due to the high level energy to strong current induced decoherences in both dots is clearly visible at  $V \approx \pm\delta$  in Figure 6.

Neglecting the finite orbital splitting, we can also get the higher order asymptotic behavior for the decoherence rates analogous to Ref. 15:

$$\gamma_i \sim \frac{\pi}{4} \frac{V}{(\ln \frac{V}{T_K^0})^2} [1 + \frac{2}{\ln \frac{V}{T_K^0}} + \dots]. \quad (21)$$

The numerical results for the different electron occupation of the two orbitals is shown in Figure 7 for different orbital splittings  $\delta$ . To ensure that the RG approach is valid, i.e., that we stay in the weak coupling regime, we use here and in the following a rather high temperature  $T/T_K^0 = 2$ . Such temperatures are actually relevant in many experiments where often the lowest accessible temperatures are of the order of the Kondo temperature. At low bias voltage  $V < \delta$ , only the lower orbital is occupied for sufficient large  $\delta$ , as is to be expected for  $\delta \gg T$ . At high bias voltage  $V > \delta$ , the electrons tend to stay in both dots with the same probability;  $\langle n_1 - n_2 \rangle$  decreases with increasing  $V$ .

The physical observable of interest, the differential conductance through the two dots  $G_i = \partial I_i(V)/\partial V$  ( $i = 1, 2$ ), is presented in Figure 8. The conductance consists of the intra-dot spin scattering and the inter-dot orbital scattering. For  $\delta = 0$ , a pronounced peak is found at  $V = 0$ , characteristic of the orbitally enhanced Kondo effect. The flow to strong coupling is, however, cut off by temperature. If the orbital degeneracy is lifted, the peak at  $V = 0$  is suppressed. For dot 2, it finally disappears at large  $\delta$  when this dot is depopulated. For dot 1, we still have a spin Kondo effect at large  $\delta$ , but with a very much reduced Kondo temperature  $T_K^{\text{SU}(2)} \ll T_K^0$ . Because also  $T_K^{\text{SU}(2)} \ll T$ , the peak at  $V = 0$  is very much smeared out. At finite  $\delta$ , two new peaks occur at  $V = \pm\delta$ , corresponding to orbital scattering. For  $T/T_K^0 = 2$ , we study an interplay between temperature-induced decoherence and current-induced decoherence. For small  $\delta$  and  $V$  the decoherence is solely due to temperature, whereas for larger

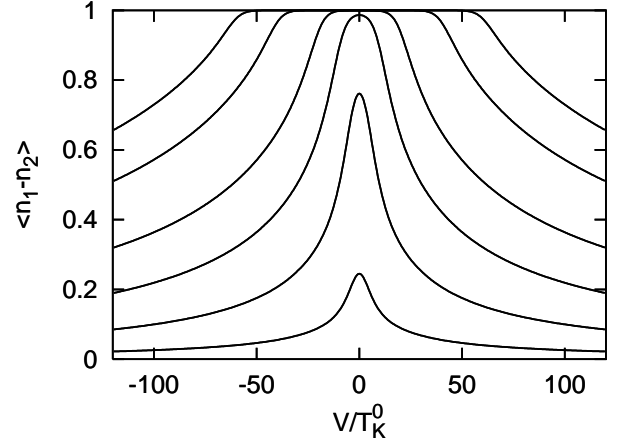


FIG. 7: Difference of the occupation of the two orbitals,  $\langle n_1 - n_2 \rangle$ , vs. bias voltage  $V$  at different orbital splitting  $\delta/T_K^0 = 60, 40, 20, 10, 4, 1$  (from top to bottom), temperature  $T/T_K^0 = 2$ , and symmetric bare couplings  $g_i^{\lambda\lambda'} = 0.04$ ,  $g_{12}^{\lambda\lambda'} = 0.06$ .

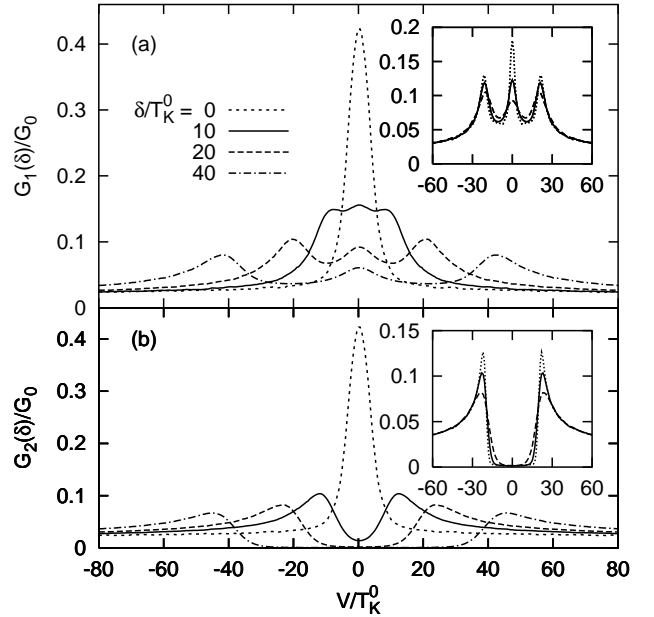


FIG. 8: Differential conductance  $G_i$  vs. bias voltage  $V$  for symmetric initial couplings  $g_i^{\lambda\lambda'} = 0.04$ ,  $g_{12}^{\lambda\lambda'} = 0.06$ , temperature  $T/T_K^0 = 2$ , and different orbital splittings  $\delta$ . Here and in the following figures,  $G_0 = 2\frac{e^2}{h}$  denotes the conductance quantum. Inset: temperature dependence of the differential conductance for  $\delta/T_K^0 = 20$  ( $T/T_K^0 = 2$ : dashed line;  $T/T_K^0 = 1$ : solid line;  $T/T_K^0 = 0.1$ : dotted line).

the voltages it is mainly current noise. For the  $\delta = 20$  and  $\delta = 40$  curves in Figure 8, the  $\gamma_1$  decoherence rate is at least at the smaller voltages temperature-induced. In contrast, the important inter-orbital decoherence rate  $\gamma_{12}$  and also  $\gamma_2$  are not even for smaller voltages.

If we decrease temperature, the main driving source for decoherence is the voltage-induced current noise. The change with temperature is studied in the inset of Figure

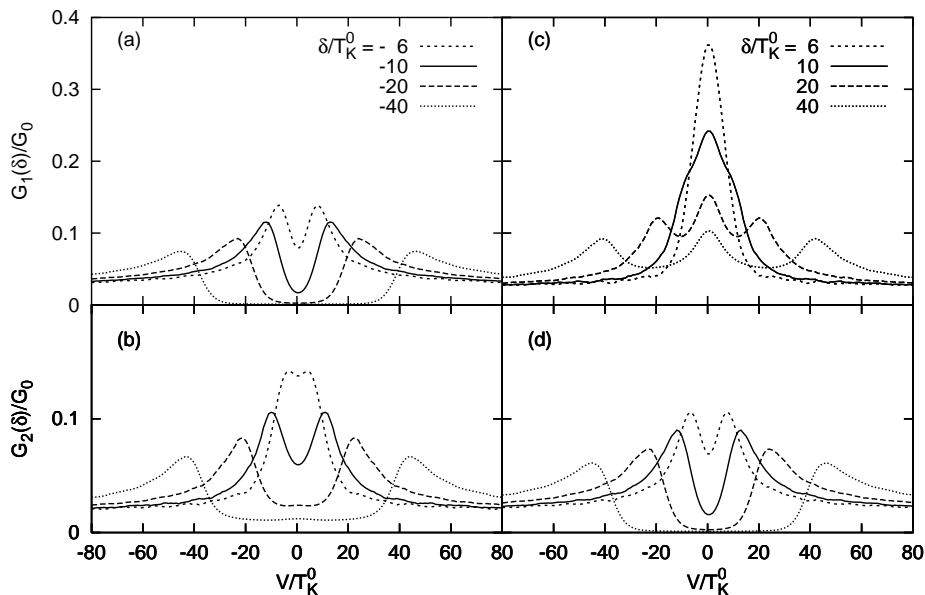


FIG. 9: Differential conductance  $G_i$  vs. bias voltage  $V$  for symmetric initial couplings  $g_1^{\lambda\lambda'} = 0.04$ ,  $g_2^{\lambda\lambda'} = 0.01$ ,  $g_{12}^{\lambda\lambda'} = 0.06$ , temperature  $T/T_K^0 = 2$ , and different orbital splittings  $\delta$ .

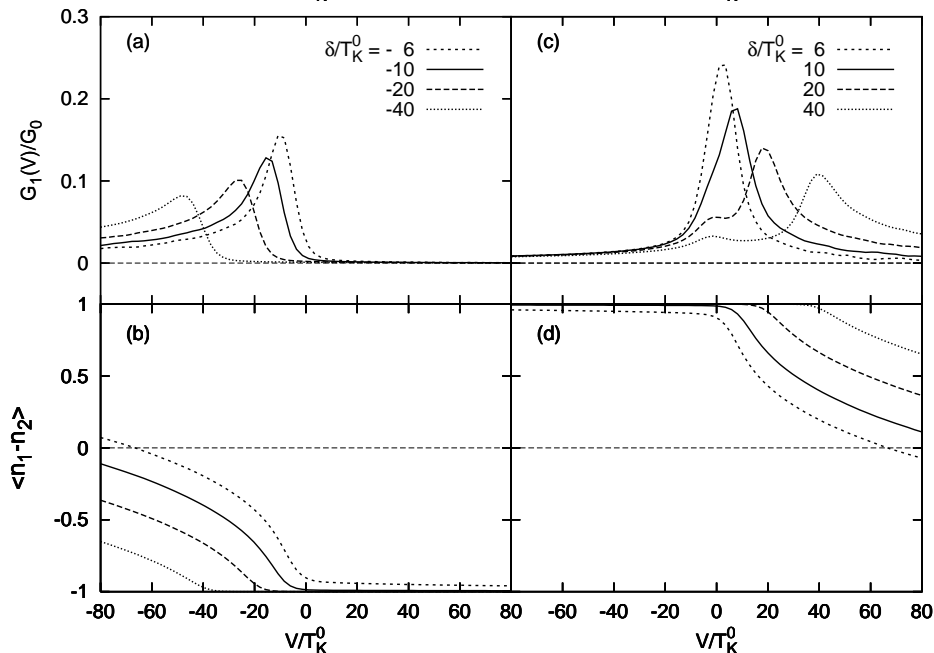


FIG. 10: Part (a) and (c) are the same as in Figure 9 but now for asymmetric initial couplings  $g_1^{LL} = 0.04$ ,  $g_1^{RR} = 0.01$ ,  $g_2^{LL} = 0.01$ ,  $g_2^{RR} = 0$ , and  $g_{12}^{LL} = 0.12$ . The Kondo peak at  $V = -\delta$  is now missing. Instead of the conductance  $G_2$  which is zero, part (b) and (d) show the difference in the occupation of the two dots.

8, showing the sharpening of the Kondo peaks. At the lowest temperature  $T/T_K^0 = 0.1$ , we reached the limit where the voltage-induced decoherence is dominating everywhere, except for the central peak in Figure 8a).

In Figure 9, we show how the conductances change if the couplings of the two dots to the leads are different. In part c) and d), the stronger coupled dot (dot 1) is lower in energy. The emerging single-dot (spin) Kondo effect at  $V \approx 0$  is somewhat suppressed, see Figure 9 c). In contrast in part a) and b), it is the weaker coupled dot which is lower in energy (dot 2). Then the spin Kondo peak for dot 2 is hardly discernible, see Figure 9 d).

In the experiments of Ref. 4, the inter-dot Coulomb interaction  $U_{12}$  is much smaller than the intra-dot Coulomb interaction  $U_{ii}$ . Hence, the initial inter-dot coupling is stronger  $g_{12}(\sim \frac{1}{U_{12} + \epsilon_d} - \frac{1}{\epsilon_d}) > g_i(\sim \frac{1}{U_{ii} + \epsilon_d} - \frac{1}{\epsilon_d})$ , as in

Figures 8 and 9.

And, as in Figures 8 and 9 b), the single-dot (spin) Kondo peak at  $V = 0$  is much weaker (if at all discernible) than the pronounced orbital Kondo peaks at  $V \approx \pm\delta$ .

### C. Asymmetric coupling to leads

Let us now discuss the situation of strongly different (initial/unrenormalized) couplings  $g_{m_1 m_2}^{\lambda_1 \lambda_2}$  to the right and the left lead:  $g_{m_1 m_2}^{RR} \neq g_{m_1 m_2}^{LL}$ . This is typically the case in experiments,<sup>4</sup> and can in extreme cases give rise to a very different physical behavior compared to that of the symmetric coupling cases.

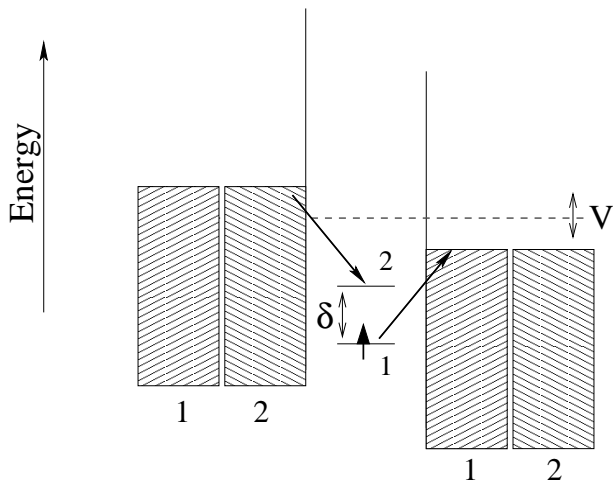


FIG. 11: Scattering process which connects the Fermi energy of the left lead (at  $+V/2$ ) and dot 2 (upper level) and that of the right lead (at  $-V/2$ ) with dot 1 (lower level); there is a separate Fermi level for each dot as indicated. The process displayed results, together with the reverse scattering process, in a Kondo resonance at  $V \approx \delta$ . For  $V > \delta$  the scattering process shown is still possible but not the reverse one.

In Ref. 4, this asymmetry is even so strong that one of the dots is effectively decoupled from the right lead ( $g_{2(12)}^{RR} = g_{2(12)}^{LR} = 0$ ), albeit still coupled to the left lead via  $g_2^{LL}$ . Such a situation is shown in Figure 10. Since dot 2 is decoupled from the left lead, the orbital Kondo effect is now only possible at  $V = +\delta$ , not any longer at  $V = -\delta$ . This can be understood by means of Figure 11. At  $V = +\delta$ , we can move an electron from the Fermi energy of the left lead into dot 2 and, conserving energy, the electron from dot 1 to the Fermi energy of the right lead, and vice versa. In the RG equations we hence get large couplings, resulting in an orbital Kondo peak. If the coupling to the leads was symmetric we could have similar scattering processes moving the electron from dot 2 to the right lead's Fermi energy and an electron from the left lead's Fermi energy to dot 1 at  $V = -\delta$ . However, since  $g_{2(12)}^{RR} = 0$  this second scattering process is not possible, as was already argued in Ref. 4. Therefore, instead of two conductance peaks as in Figures 8 and 9 we see only one at  $V = +\delta$  in Figure 10, which presents results for such strongly asymmetric couplings. The nearly indiscernible spin Kondo peak and the missing peak at  $V \approx -\delta$  qualitatively agree with experiments.<sup>4</sup> As for symmetric coupling, the height of the orbital Kondo peak at  $V = \pm\delta$  decreases with increasing  $\delta$ .

An interesting phenomena in the case of asymmetric couplings occurs if  $g_2^{RR} = 0$  as before but  $g_1^{RR} \gg g_1^{LL}$ : As shown in Figure 12, we find a negative differential conductance which is always present after the orbital Kondo peak, i.e., for  $V > \delta$ . Generally such negative conductances occur when the hopping parameters of the Anderson model fulfill  $|t_{R1}| \gg |t_{L1}|$ ,  $|t_{R2}| \ll |t_{L2}|$ . How can we

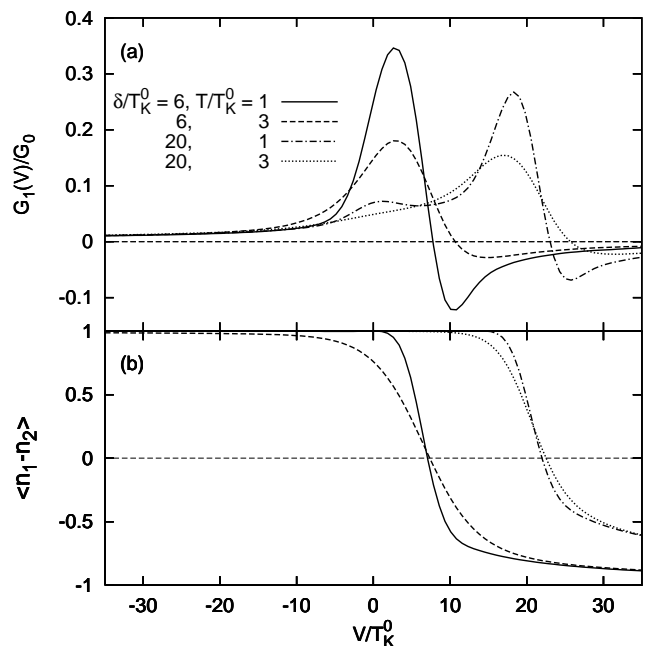


FIG. 12: Same as on the right hand side of Figure 10 but now for  $g_1^{LL} = 0.01 < g_1^{RR} = 0.04$ , and  $g_{12}^{LL} = 0.01$ ,  $g_1^{RR} = 0$  as before); shown are two different values of  $\delta$  and temperature. For these parameters, the differential conductance is negative after the Kondo peak at  $V \approx \delta$  which can be explained by the inversion of the occupation numbers, shown in part (b).

understand this unexpected negative conductance?

The basic picture is that –although higher in energy– dot 2 is increasingly occupied for  $V > \delta$ . Counterintuitively, it becomes even more occupied than dot 1, see the lower part of Figure 12. The reason for this inversion of the occupation (in comparison to the equilibrium occupation) can be understood from the sketch in Figure 11. The scattering process shown in the Figure is energetically possible: Because  $V - \delta > 0$ , we can transfer an electron from the Fermi level of the left lead to the empty states above the Fermi level of the right lead and still pay the energy  $\delta$  to change the local state from dot 1 to dot 2. But the reverse process, starting with an electron from the right lead's Fermi level, is not possible since  $\delta - V < 0$ . All the other processes for changing the local state back from dot 2 to dot 1 are much smaller because of  $|t_{L1}|/|t_{R1}| \ll 1$  and  $|t_{R2}|/|t_{L2}| \ll 1$ . Take for example the process involving the transfer of the dot 2 electron to the right lead and simultaneously that of an electron from the left lead to dot 1. The amplitude for this process is by a factor of  $|g_{12}^{LR}/g_{21}^{LR}|$  ( $\approx |t_{L1}/t_{R1}| |t_{R2}/t_{L2}| \ll 1$ ) smaller than that of Figure 10. Hence, the localized state is nearly trapped in dot 2,  $\langle n_1 - n_2 \rangle < 0$ , for large bias voltage.

Altogether the behavior of the conductance in Figure 12 can be explained as following: At  $V \approx \delta$  a new, inter-orbital channel opens for conductance to the left lead of dot 1, the one displayed in Figure 11. This explains the

strong enhancement of  $G_1$  for  $V \approx \delta$ ; the orbital Kondo peak in Figure 12. With a further increase of  $V$ , however, there is a dramatic decrease of  $\langle n_1 - n_2 \rangle$  and hence of the number of electrons in dot 1 ( $\langle n_1 \rangle$ ). Because of this, the contribution to the current involving solely dot 1, i.e., the first line in Eq. (9), rapidly decreases. This decrease dominates for  $V > \delta$ , resulting in a negative differential conductance.

Negative conductances for quantum dots with many levels have been observed experimentally<sup>27</sup> and described theoretically,<sup>28</sup> albeit in the sequential tunneling regime. Our results show that similar effects are also possible in the Kondo regime.

#### D. Linear conductance

Substantial simplifications arise in the linear response regime for small voltages since there are no nonequilibrium effects any more like the current induced decoherence rate  $\gamma_i$  and the frequency dependence of the vertex. This linear conductance can be used as an indicator whether we have a spin or an orbital Kondo effect, corresponding to the limits  $g_i \gg g_{12}$  and  $g_{12} \gg g_i$ , respectively. In both cases, the linear conductance for dot 1 increases at  $\delta \approx 0$ , since then dot 1 becomes occupied and conducting. But while at larger values of  $\delta$  ( $\delta/T_K^0 \gg 1$ ) the spin Kondo effect still works, the orbital Kondo effect breaks down in the linear conductance regime. In Figure 13 a), the conductance has hence a plateau form in the former case, while it has a peak form for the orbital Kondo effect. The reason for this dramatic decrease of the conductance is simply that the RG flow of the inter-orbital coupling (and that for the high energy dot) is cut-off at an energy scale  $\sim \delta$ , preventing a strong renormalization and, hence, suppressing the conductance at larger values of  $\delta$ .

This different behavior allows us to identify the change of the conductance with  $\delta$ , i.e.,  $\partial G(\delta)/\partial \delta$ , as a good candidate to determine whether we have a spin or orbital Kondo effect. As Figure 13 b) shows, this quantity is symmetric for the spin Kondo effect but asymmetric for the orbital Kondo effect. Note, that  $\partial G(\delta)/\partial \delta$  is often accessible experimentally; the two dots need only be controllable by different gate voltages for changing  $\delta$ .

## IV. CONCLUSION

In conclusion, we reported on the extension of the nonequilibrium perturbative RG scheme to multi-orbital applications. The method keeps the simplicity of the poor man's scaling approach, but can be used for nonequilibrium transport by including the frequency dependence of the vertex. However, it is restricted to the weak coupling regime. Either current or temperature has to cut off the flow to the strong coupling fix point.

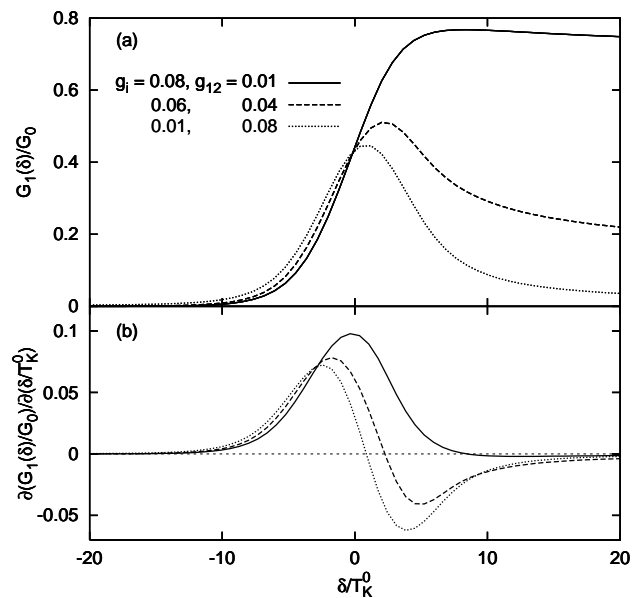


FIG. 13: Part (a): Linear conductance  $G_1(\delta)$  as a function of orbital splitting  $\delta$  for symmetric coupling (see legend;  $T/T_K^0 = 2$ , note that  $T_K^0$  depends on  $g$ ). Part (b) shows  $\partial G_1(\delta)/\partial \delta$  vs.  $\delta$  which is symmetric/antisymmetric for a predominantly spin/orbital Kondo effect.

Specifically, we calculated conductances for the case of two quantum dots coupled only electrostatically. For SU(2) spin symmetry one spin (at  $V \approx 0$ ) and two orbital Kondo peaks (at  $V \approx \pm \delta$ ) are found, in agreement with the expectations. For the typical experimental situation that the intra-dot Coulomb interaction is much stronger than the inter-dot Coulomb interaction (translating to initial couplings  $g_{12} \gg g_1, g_2$ ) however, the spin Kondo peak is much less pronounced, if at all discernible.

For strongly asymmetric couplings with the extreme situation that one of the dots is decoupled from one of the two leads, the conductance peak at  $V \approx -\delta$  disappears, as observed experimentally.<sup>4</sup> An unexpected result was the negative differential conductance immediately after the remaining Kondo peak at  $V \approx \delta$ , occurring for initial couplings  $g_1^{RR} \gg g_1^{LL}$  and  $g_2^{RR} \ll g_2^{LL}$ . This is a genuine nonequilibrium phenomenon.

Already in the linear conductance regime, we can distinguish between spin and orbital Kondo effect via the derivative  $\partial G_i(\delta)/\partial \delta$  which is symmetric and antisymmetric w.r.t.  $\delta \rightarrow -\delta$ , respectively.

#### Acknowledgments

We thank A. Hübner, A. A. Katanin, A. Rosch, D. Quirion, and J. Weis for discussions. This work was supported in part by the Deutsche Forschungsgemeinschaft through the Emmy Noether program.

\*

## APPENDIX A: DECOHERENCE RATES

In this Appendix, we calculate the decoherence rates via the susceptibility or the corresponding correlation function:

$$\chi_{m_1 m_2}(\omega) = \langle\langle X^{m_1 m_2}; X^{m_2 m_1} \rangle\rangle_\omega, \quad (\text{A1})$$

where  $\langle\langle A; B \rangle\rangle = -i\Theta(t)\langle[A(t), B]\rangle$  and  $\langle\langle \dots \rangle\rangle_\omega$  denotes the Fourier transformation to frequency space.

Near resonance  $\omega_0$ ,  $\chi_{m_1 m_2}(\omega)$  behaves like:

$$\chi_{m_1 m_2}(\omega) \sim \frac{1}{(\omega - \omega_0) + i\gamma_{m_1 m_2}}, \quad (\text{A2})$$

where  $\gamma_{m_1 m_2}$  is just the decoherence rate wanted.

For the exact diagrammatic evaluation at finite bias voltage, one should consider the whole Keldysh contour like in Ref. 16. However, for the lowest order contribution, it is sufficient to use only the equilibrium Green functions as in Ref. 17. Moreover, the proper decoherence rates to the lowest order in  $J$  can be obtained from the equation of motion method like in Ref. 29 with a truncation of the Eqs. in second order in  $J$ .

The equation of motion of the correlation functions for Hamiltonian (3) is written as:

$$\begin{aligned} \omega \chi_{m_1 m_2}(\omega) &= \langle[X^{m_1 m_2}, X^{m_2 m_1}]\rangle + \langle\langle[X^{m_1 m_2}, H]; X^{m_2 m_1}\rangle\rangle_\omega \\ &= \langle X^{m_1 m_1} - X^{m_2 m_2} \rangle + (\epsilon_{m_2} - \epsilon_{m_1}) \langle\langle X^{m_1 m_2}; X^{m_2 m_1} \rangle\rangle_\omega \\ &+ \sum_{\lambda k; \lambda' m' k'} J_{m_2 m'}^{\lambda \lambda'} \langle\langle X^{m_1 m'} c_{\lambda' m' k'}^+ c_{\lambda m_2 k}; X^{m_2 m_1} \rangle\rangle_\omega \\ &- \sum_{\lambda m k; \lambda' k'} J_{m m_1}^{\lambda \lambda'} \langle\langle X^{m m_2} c_{\lambda' m_1 k'}^+ c_{\lambda m k}; X^{m_2 m_1} \rangle\rangle_\omega \\ &+ \sum_{\lambda k; \lambda' m' k'} (\tilde{J}_{m_2 m'}^{\lambda \lambda'} - \tilde{J}_{m_1 m'}^{\lambda \lambda'}) \langle\langle X^{m_1 m_2} c_{\lambda' m' k'}^+ c_{\lambda m' k}; X^{m_2 m_1} \rangle\rangle_\omega. \end{aligned}$$

$$\begin{aligned} B_{m_1 m_2}(\omega) &= \rho_0 \sum_{\lambda \lambda' k m} \{ J_{m_1 m}^{\lambda' \lambda} J_{m m_1}^{\lambda \lambda'} f_\lambda(\epsilon_k) [1 - f_{\lambda'}(\epsilon_k - \omega + \tilde{\epsilon}_{m_2} - \tilde{\epsilon}_{m_1})] + [\tilde{J}_{m_1 m}^{\lambda' \lambda} (\tilde{J}_{m_1 m}^{\lambda \lambda'} - \tilde{J}_{m_2 m}^{\lambda \lambda'}) + \delta_{m m_2} J_{m_1 m_1}^{\lambda' \lambda} \\ &(2\tilde{J}_{m_1 m_1}^{\lambda \lambda'} - \tilde{J}_{m m_1}^{\lambda \lambda'}) - \delta_{m m_2} J_{m_2 m_2}^{\lambda' \lambda} \tilde{J}_{m_1 m_1}^{\lambda \lambda'}] f_\lambda(\epsilon_k) [1 - f_{\lambda'}(\epsilon_k - \omega + \tilde{\epsilon}_{m_2} - \tilde{\epsilon}_{m_1})] \} + (m_1 \leftrightarrow m_2, \omega \rightarrow -\omega), \quad (\text{A6}) \\ C_{m_1}^m(\omega) &= \rho_0 \sum_{\lambda \lambda' k} J_{m m_1}^{\lambda' \lambda} J_{m_1 m}^{\lambda \lambda'} f_\lambda(\epsilon_k) (1 - f_{\lambda'}(\epsilon_k + \omega + \tilde{\epsilon}_m - \tilde{\epsilon}_{m_1})) + (\omega \rightarrow -\omega). \end{aligned}$$

For  $m_1 \neq m_2$ , we directly obtain the decoherence rate from Eq. (A5), taking  $\omega \rightarrow \omega_0 \approx \tilde{\epsilon}_{m_2} - \tilde{\epsilon}_{m_1}$ :

$$\gamma_{m_1 m_2} = \pi B_{m_1 m_2}(\omega_0). \quad (\text{A7})$$

This is the rate entering the RG Eq. (6) as a cut-off. In our perturbative RG calculation, we replace the bare couplings  $\rho_0 J$  by the renormalized  $g(\omega)$ 's in Eq. (A6). Then, scaling corrections are included in a similar way as in the RG Eqs. themselves.

Here, we used the fact that  $X^{m_1 m_2} X^{m_3 m_4} = \delta_{m_2 m_3} X^{m_1 m_4}$  in the single electron subspace. The terms on the right hand side can be expressed in a similar way by another equation of motion. We then decouple this equation of motion by using the approximation

$$\begin{aligned} \langle\langle X^{m_1 m_2} c_1^+ c_2^+ c_3^+ c_4; X^{m_2 m_1} \rangle\rangle_\omega &\approx \\ &[(c_2 c_3^+) \langle c_1^+ c_4 \rangle + \langle c_1^+ c_2 \rangle \langle c_3^+ c_4 \rangle] \langle\langle X^{m_1 m_2}; X^{m_2 m_1} \rangle\rangle_\omega. \quad (\text{A3}) \end{aligned}$$

This way, we neglect terms to order  $J^3$ , i.e., our decoherence rate is only valid to order  $J^2$ . The  $\langle c_1^+ c_2 \rangle \langle c_3^+ c_4 \rangle$  term can be absorbed in a renormalization of the energies

$$\epsilon_m \rightarrow \tilde{\epsilon}_m \approx \epsilon_m + \sum_{\lambda k} [J_{m m}^{\lambda \lambda} f_\lambda(\epsilon_k) + \sum_{m'} \tilde{J}_{m m'}^{\lambda \lambda} f_\lambda(\epsilon_k)]. \quad (\text{A4})$$

We can effectively include this renormalization by denoting with  $\epsilon_m$  not the original level energy of the Hamiltonian but the renormalized  $\tilde{\epsilon}_m$  which is also measured in the experiment. The RG Eqs. would include the same kind of change if higher order terms were included.

$$\begin{aligned} (\omega + \epsilon_{m_1} - \epsilon_{m_2}) \chi_{m_1 m_2}(\omega) &= \langle X^{m_1 m_1} - X^{m_2 m_2} \rangle \\ &- i\pi B_{m_1 m_2}(\omega) \chi_{m_1 m_2}(\omega) \\ &+ i\pi \delta_{m_1 m_2} \sum_m C_{m_1}^m(\omega) \langle\langle X^{m m}; X^{m_1 m_1} \rangle\rangle_\omega \quad (\text{A5}) \end{aligned}$$

plus an additional real part which typically results in a modification of  $\tilde{\epsilon}$  but is of no interest for the decoherence rates since these correspond to the imaginary part given by

For  $m_1 = m_2$ , the last term in Eq. (A5) cannot be neglected. The calculation becomes slightly more difficult since a corresponding equation for  $\langle\langle X^{m m}; X^{m_1 m_1} \rangle\rangle_\omega$  (the terms entering the longitudinal susceptibility) is needed. However, often, one does not need the  $m_1 = m_2$  decoherence rate explicitly. For example, the calculations of the paper are for a SU(2) spin symmetry for both levels/dots. Then, the longitudinal susceptibility and decoherence rate  $\gamma_{m_1 m_1}$  with  $m_1 = \{i, \sigma\}$  is simply equal to

the transversal rate  $\gamma_{m_1 m_2}$  for  $m_2 = \{i, -\sigma\}$ .

As an example, the relaxation rate of the SU(N) model is

$$\gamma = 2\pi N \rho_0^2 J^2 T, \quad (\text{A8})$$

which can be obtained by simply substituting  $J_{m_1 m_2} = J$  and  $\bar{J}_{m_1 m_2} = J/N$ .

An additional check is the spin- $\frac{1}{2}$  Kondo model. In a magnetic field and at a finite bias, we obtain from Eq. (A5) and an analogous equation of motion for  $\langle\langle X^{mm}; X^{m_1 m_1} \rangle\rangle_\omega$  the transversal and longitudinal spin relaxation rates:

$$\begin{aligned} \gamma_\perp = \frac{\pi}{4} \rho_0^2 J^2 \sum_{\lambda\lambda's} \int d\epsilon [f_\lambda(\epsilon - \frac{s\delta}{2})(1 - f_{\lambda'}(\epsilon + \frac{s\delta}{2})) \\ + f_\lambda(\epsilon)(1 - f_{\lambda'}(\epsilon))], \quad (\text{A9}) \end{aligned}$$

$$\gamma_\parallel = \frac{\pi}{2} \rho_0^2 J^2 \sum_{\lambda\lambda's} \int d\epsilon [f_\lambda(\epsilon - \frac{s\delta}{2})(1 - f_{\lambda'}(\epsilon + \frac{s\delta}{2}))]. \quad (\text{A10})$$

This is just the lowest order results one expects from nonequilibrium perturbation theory<sup>16</sup>, i.e.:

$$\gamma_\perp \approx \gamma_\parallel \approx 4\pi \rho_0^2 J^2 \max\{T, \frac{V}{4}\} \quad (\text{A11})$$

for  $\max\{V, T\} \gg \delta$ , and

$$\gamma_\perp \approx \frac{\gamma_\parallel}{2} \approx \pi \rho_0^2 J^2 \delta \quad (\text{A12})$$

for  $\max\{V, T\} \ll \delta$ .

- 
- <sup>1</sup> See, e.g., L. I. Glazman and M. E. Raikh, Pis'ma Zh. Éksp. Teor. Fiz. **47**, 378 (1988) [Sov. Phys. JETP Lett. **47**, 452 (1988)]; T. K. Ng and P. A. Lee, Phys. Rev. Lett. **61**, 1768 (1988); S. Hershfield, J. H. Davies, and J. W. Wilkins, Phys. Rev. Lett. **67**, 3720 (1991); Phys. Rev. B **46**, 7046 (1992); J. König, J. Schmid, H. Schoeller, and G. Schön, Phys. Rev. B **54**, 16820 (1996).
- <sup>2</sup> Y. Meir, N. S. Wingreen, and P. A. Lee, Phys. Rev. Lett. **70**, 2601 (1993).
- <sup>3</sup> D. Goldhaber-Gordon, H. Shtrikman, D. Mahalu, D. Abusch-Magder, U. Meirav, and M. A. Kastner, Nature **391**, 156 (1998); S. M. Cronenwett, T. H. Oosterkamp, and L. P. Kouwenhoven, Science **281**, 540 (1998); J. Schmid, J. Weis, K. Eberl, and K. v. Klitzing, Physica B **256-258**, 182 (1998).
- <sup>4</sup> U. Wilhelm and J. Weis, Physica E **6**, 668 (2000); U. Wilhelm, J. Schmid, J. Weis, and K. v. Klitzing, Physica E **9**, 625 (2001); **14**, 385 (2002).
- <sup>5</sup> J. R. Schrieffer and P. A. Wolff, Phys. Rev. **149**, 491 (1966).
- <sup>6</sup> B. Coqblin and J. R. Schrieffer, Phys. Rev. **185**, 847 (1969).
- <sup>7</sup> In second order scaling theory [one-loop perturbative renormalization group (RG)] the prefactor is given by the conduction electron bandwidth  $D$  of the Coqblin-Schrieffer model. It gets corrected by a factor  $(N\rho_0 J)^{(1/N)}$  in third order scaling theory or when calculating the Anderson impurity model exactly by Bethe ansatz.<sup>8</sup>
- <sup>8</sup> A. C. Hewson, *The Kondo Problem to Heavy Fermions*, Cambridge University Press (Cambridge, 1993).
- <sup>9</sup> See, e.g., T. Pohjola, J. König, M. M. Salomaa, J. Schmid, H. Schoeller, and G. Schön, Europhys. Lett. **40**, 189 (1997); T. Pohjola, H. Schoeller, and G. Schön, Europhys. Lett. **54**, 241 (2001); D. Boese, W. Hofstetter, and H. Schoeller, Phys. Rev. B **64**, 125309 (2001); W. Izumida, O. Sakai, S. Tarucha, Phys. Rev. Lett. **87**, 216803 (2001).
- <sup>10</sup> W. Izumida, O. Sakai, and Y. Shimizu, J. Phys. Soc. Jap. **67**, 2444 (1998).
- <sup>11</sup> D. Boese, W. Hofstetter, H. Schoeller, Phys. Rev. B **66**, 125315 (2002).
- <sup>12</sup> L. Borda, G. Zaránd, W. Hofstetter, B. I. Halperin, and J. von Delft, Phys. Rev. Lett. **90**, 026602 (2003).
- <sup>13</sup> M. Eto, cond-mat/0408159 (unpublished).
- <sup>14</sup> J. Ye, Phys. Rev. B **56**, R489 (1997).
- <sup>15</sup> A. Rosch, J. Kroha, and P. Wölfle, Phys. Rev. Lett. **87**, 156802 (2001).
- <sup>16</sup> J. Paaske, A. Rosch, J. Kroha and P. Wölfle, Phys. Rev. B **70** 155301 (2004).
- <sup>17</sup> A. Rosch, J. Paaske, J. Kroha, and P. Wölfle, Phys. Rev. Lett. **90**, 076804 (2003); J. Phys. Soc. Jap. **74**, 118 (2005); A. Rosch, T. A. Costi, J. Paaske, and P. Wölfle, Phys. Rev. B **68**, 014430 (2003).
- <sup>18</sup> Let us also call the reader's attention to another nonequilibrium scaling approach, using the flow equation method: S. Kehrein, cond-mat/0410341 (unpublished).
- <sup>19</sup> P. W. Anderson, J. Phys. C **3**, 2436 (1970).
- <sup>20</sup> J. Hubbard, Proc. Roy. Soc. A **285**, 542 (1965).
- <sup>21</sup> L. V. Keldysh, Zh. Éksp. Teor. Fiz. **47**, 1515 (1964) [Sov. Phys. JETP **20**, 1018 (1965)], J. Rammer and H. Smith, Rev. Mod. Phys. **58**, 323 (1986).
- <sup>22</sup> J. Paaske, A. Rosch, and P. Wölfle, Phys. Rev. B **69**, 155330 (2004).
- <sup>23</sup> A difference to Ref. 17 is the way how we deal with the frequency conservation at the two vertices of Figure 1. In Ref. 17, the conduction electron frequency of the intermediate state is set to the band edge  $\omega' = \pm D$  so that the pseudo Fermion line (dashed line in Figure 1) is off resonance, i.e., its frequency  $\neq \epsilon_m$  where  $m$  is the intermediate pseudo Fermion (localized) state. In contrast in Eq. (6), the localized state is on resonance at  $\epsilon_m$  so that the conduction electron frequency  $\omega' \neq D$ . This is similar to the traditional poor man's scaling approach where  $\omega' \neq D$  and the conduction electron momentum is such that  $\epsilon_k = \pm D$ , see, e.g. Ref. 8 for details.
- <sup>24</sup> This is the Kondo temperature which the two dot system had if the orbital splitting was zero but the  $g$ 's were the same. The reason for taking  $T_K(\delta = 0)$  as the energy unit is to study changes w.r.t.  $\delta$ , keeping the other parameters constant.
- <sup>25</sup> See, e.g., M. Pustilnik and L. I. Glazman, Phys. Rev. B **64**, 045328 (2001).
- <sup>26</sup> More details on this issue will be discussed in A. Rosch, J.

- Paaske, J. Kroha, and P. Wölfle (unpublished).
- <sup>27</sup> A. T. Johnson, L. P. Kouwenhoven, W. de Jong, N. C. van der Vaart, C. J. P. M. Harmans, and C. T. Foxon, Phys. Rev. Lett. **69**, 1592 (1992); J. Weis, R. J. Haug, K. v. Klitzing, and K. Ploog, Phys. Rev. Lett. **71**, 4019 (1993).
- <sup>28</sup> D. Weinmann, W. Häusler, and B. Kramer, Ann. Physik (Leipzig) **5**, 652 (1996); M. H. Hettler, H. Schoeller, and W. Wenzel, Europhys. Lett. **57**, 571 (2002); G. Michałek and B. R. Bułka, Eur. Phys. J. B **28**, 121 (2002).
- <sup>29</sup> W. Götze and P. Wölfle, J. Low Temp. Phys. **5**, 575 (1971).